V International Conference on Particle-based Methods – Fundamentals and Applications
PARTICLES 2017
P. Wriggers, M. Bischoff, E. Oñate, D.R.J. Owen, & T. Zohdi (Eds)

MECHANICAL BEHAVIOR OF BOUNDARY LAYER IN DISCRETE MODELS BASED ON VORONOI TESSELLATION

Jan Eliáš[1]

[1] Brno University of Technology
Faculty of Civil Engineering, Institute of Structural Mechanics
Veveří 331/95, Brno, 602 00, Czech Republic
jan.elias@vut.cz; http://www.fce.vutbr.cz/stm/elias.j/

Key words: discrete model, boundary layer, wall effect, concrete, elasticity, fracture

Abstract. The contribution introduces 2D and 3D discrete static model of concrete based on Voronoi tessellation. Attention is focused on the boundary region where, due to presence of boundaries, the orientation of contacts exhibits strong bias. The bias has consequences in mechanical behavior of the boundary region in both elastic and inelastic regimes. The boundary layer is typically weaker and more brittle compared to the interior and also stiffer or more compliant depending on macroscopic Poisson's ratio and straining direction.

1 INTRODUCTION

This contribution is a promotion of the recent journal paper [1], particular results and conclusions of the paper are shown in this contribution.

Solid matter occupies spatial domains defined by boundaries. It is known that there exists a layer in the vicinity of the boundary where the material properties might differ from the interior. The boundary layer might be result of several effects, for example actions of external environment. In concrete, the boundary layer typically differs also in grain size distribution having increased amount of small grains and mortar compared to the interior material [2]. The boundary layer of different material properties compared to interior affects mechanical behavior of concrete solids.

When simulating the concrete members, the boundary layer is typically not explicitly addressed (but exceptions exist, see e.g. [3]). However, it might be imposed by the nature of the model. This can be seen for example when using nonlocal models [4], which naturally create boundary layer of different behavior. The contribution shows that this is also the case of discrete models. Their mechanical behavior relies on discretization of a solid domain into particles with random irregular composition, but presence of the bound-

aries affects the irregularity and produces some boundary layer with different statistical distributions of geometrical variables.

However, the contact constitutive behavior of discrete models can also be developed to become completely independent on the geometry of the rigid bodies. It has been achieved both for elastic behavior [5, 6, 7] and inelastic behavior [8]. In such a case, the boundary layer has no mechanical consequences. In majority of the discrete models, the contact behavior take into account the geometry of the contact in both linear and nonlinear regimes and therefore the boundary layer is active.

Comparison of the boundary layer and interior tessellation geometry and stress is presented in the contribution. Due to unbiased behavior of the interior, analytical formulas can be developed for its macroscopic elastic behavior. The real mechanical behavior of the discrete system is compared with these analytical predictions. Most of the comparison is done via statistical characteristics called the mean value and standard deviation. Having some function $G = g(\gamma)$ dependent on random variable γ with probability density function $f(\gamma)$, the mean value, μ_G, and standard deviation, δ_G, is defined as

$$\mu_G = \int_{-\infty}^{\infty} g(\gamma) f_\gamma(\gamma) \mathrm{d}\gamma \qquad \delta_G = \sqrt{\int_{-\infty}^{\infty} (g(\gamma) - \mu_G)^2 f_\gamma(\gamma) \mathrm{d}\gamma} \tag{1}$$

2 GEOMETRY OF THE DISCRETE STRUCTURE

The studied model is a discrete system of rigid bodies connected at common facets by linear or nonlinear contacts. Both the 2D and 3D versions of the model are used here.

The algorithm for construction of the discrete model geometry is controlled by parameter $l_{\min}$. The domain of the simulated solid is filled with nuclei with random location in a sequential process. New nucleus is accepted only when its distance to all previously placed nuclei is lower than $l_{\min}$. The filling is terminated after a large number of subsequent rejections is detected, i.e. when the domain is saturated. Voronoi tessellation is performed to divide the domain into rigid bodies. According to [9], the nuclei are mirrored across the boundaries before performing the Voronoi tessellation. The tessellation then creates the boundaries of the rigid bodies exactly coinciding with the boundaries of the specimen (Fig. 1a).

In order to perform comparison with models without a boundary, periodic boundary conditions are used. During random placement of nuclei, every nucleus is periodically repeated twice in the y and z directions. The tessellation is then performed on a periodic structure that is $3\times$ larger in both the y and z directions. When solving the mechanical system, periodic images of nuclei have dependent DOFs and only one periodic image of each contact contributes to the strain energy and is therefore included in the stiffness matrix. This approach completely removes boundaries and creates ideal directionally unbiased geometry. The boundaries can be also inserted into the periodic structure., The nuclei in the central part of the prismatic specimen are mirrored across the xy and xz

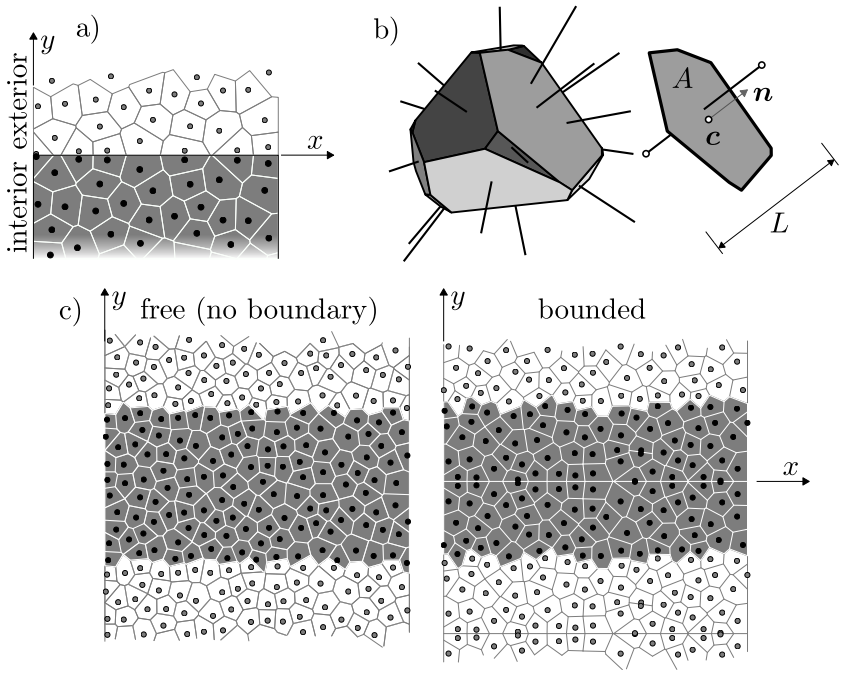

Figure 1: a) Boundary region and Voronoi tessellation on randomly placed nuclei in 2D; b) one 3D rigid body and one contact facet; c) periodic structure without and with the boundary in 2D.

plane. After tessellation, the planes xy and xz behave in the same way as the specimen boundary with directionally biased geometry in its vicinity. An example of the periodic boundary *free* and periodic *bounded* structures in 2D is shown in Fig. 1c.

Voronoi faces, here referred to as facets, represents the bonds between two bodies. The orientation of the contact facet is described by its *normal* direction, $\boldsymbol{n}$; the length of the contact is denoted $L = \|\boldsymbol{x}_a - \boldsymbol{x}_b\|$, its area is A and centroid is $\boldsymbol{c}$ (Fig. 1b).

3 CONTACT CONSTITUTIVE BEHAVIOR

The constitutive equations are taken from [10] and simplified. A full description of both linear and nonlinear constitutive equations and model kinematics is provided in [11].

Each body has three degrees of freedom in two dimensions (2×translation u, 1×rotation θ), and 6 in three dimensions (3×translation u, 3×rotation θ). Translations and rotations of the rigid bodies give rise to a displacement jump, $\boldsymbol{\Delta}$, measured at the centroid of the contact facets. The strain is measured by a scalar in the normal direction (N) and by a vector in the shear direction (T)

$$e_N = \frac{\boldsymbol{n} \cdot \boldsymbol{\Delta}}{L} \qquad \boldsymbol{e}_T = \frac{\boldsymbol{\Delta}}{L} - e_N \boldsymbol{n} \tag{2}$$

The shear strain is perpendicular to the normal direction $\boldsymbol{n}$. The stress is then calculated

based on the strain and two elastic parameters of the model, E_0 and α

$$s_N = (1-D)E_0 e_N \qquad \boldsymbol{s}_T = (1-D)E_0\alpha\boldsymbol{e}_T \tag{3}$$

Variable D is a measure of integrity loss of individual contacts called damage. When $D = 0$, the contact is intact and exhibits elastic behavior. Completely damaged element would have D equal to 1. The evolution of D is dependent on straining direction and is governed by additional model parameters, the tensile strength f_t and the fracture energy G_F. The more shear is involved, the higher the strength and energy dissipation at the facet, see [11] or directly the original model [10].

In elastic regime, one can derive simple formulas relating contact elastic parameters, E_0 and α, to the elastic parameters of isotropic homogeneous continuum, elastic modulus E and Poisson's ratio ν.

$$\begin{aligned}
&\nu = \frac{1-\alpha}{3+\alpha} && E = E_0\frac{2+2\alpha}{3+\alpha} && \text{2D, plane stress}\\
&\nu = \frac{1-\alpha}{4} && E = E_0\frac{(1+\alpha)(5-\alpha)}{8} && \text{2D, plane strain}\\
&\nu = \frac{1-\alpha}{4+\alpha} && E = E_0\frac{2+3\alpha}{4+\alpha} && \text{3D}
\end{aligned} \tag{4}$$

The derivation is based on a theory provided in [12] and its detail step-by-step explanation can be found in [1]. Three fundamental features of the tessellation are used in the derivation: (i) the normals are parallel to lines connecting two nodes in contact; (ii) there are no holes in the discrete structure, the solid is filled by the rigid bodies without any overlapping or gap; (iii) there is no directional bias in the geometry, i.e. all normal directions are equally probable and contact areas and lengths are independent on normal directions.

The first two features are automatically guaranteed by the Voronoi tessellation, while the third one depends on the process of placing the nuclei into the solid domain. It will be shown in the next section, that it is valid for the interior, but the boundary layer exhibits, due to mirroring of the nuclei in the boundary region, strong directional bias and deviation from the third assumption.

It is worth noting that equations (4) establish limitations in Poisson's ratio for discrete models. Using theoretical meaningful limits 0 and ∞ for parameter α, the maximum and minimum Poisson's ratio can be calculated as $\left(-1, \frac{1}{3}\right)$ for 2D plane stress, $\left(-\infty, \frac{1}{4}\right)$ for 2D plane strain and $\left(-1, \frac{1}{4}\right)$ for 3D model. Fortunately, representation of concrete with Poisson's ratio around 0.2 is possible in all cases.

4 DIRECTIONAL BIAS IN THE VICINITY OF BOUNDARIES

The elemental direction in the boundary layer is strongly biased towards normals aligned with the boundary. It is simply caused by the effort to create the boundary

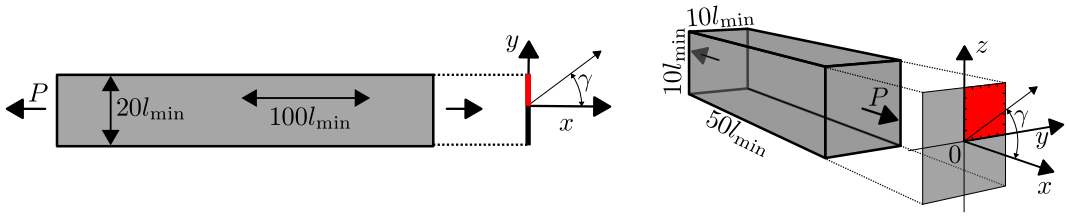

Figure 2: 2D and 3D specimens, dimensions, definition of the angular deviation γ and symmetric half or quarter of the cross-section in red.

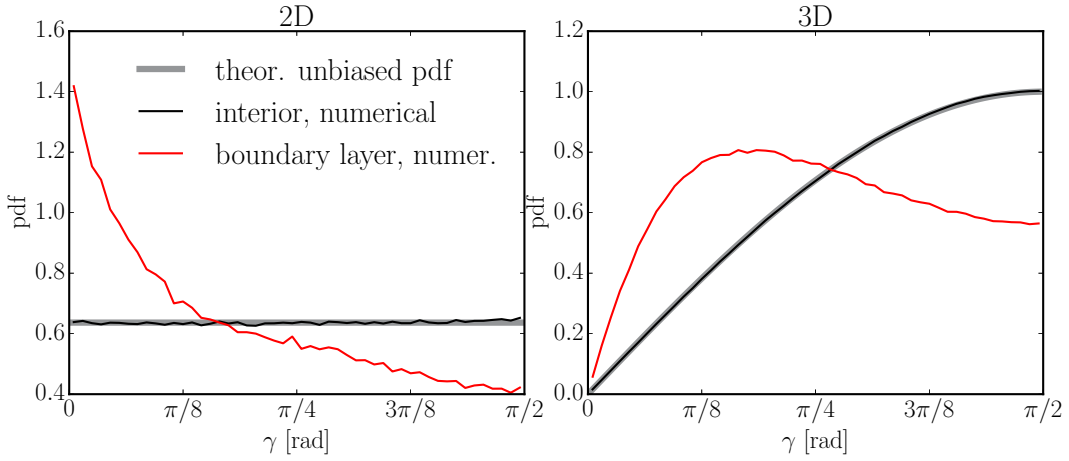

Figure 3: Probability distribution of the angular deviation from the x direction in 2D & 3D.

by the tessellation and there is no way known to the author how to reduce the effect or even get rid of it completely. The directional bias is demonstrated by variable γ, the angular deviation of the contact normal from the direction of the x axis, see Fig. 2.

The angular deviation, γ, is calculated in 2D and 3D model of prism shown in Fig. 2. In the ideal case where all the directions have the same probability, γ should have the following probability density

$$f_\gamma(\gamma) \quad \overset{\text{2D}}{=} \begin{cases} 2/\pi & \text{for } \gamma \in (0, \pi/2) \\ 0 & \text{otherwise} \end{cases} \quad \overset{\text{3D}}{=} \begin{cases} \sin(\gamma) & \text{for } \gamma \in (0, \pi/2) \\ 0 & \text{otherwise} \end{cases} \tag{5}$$

The specimens from the Fig. 2 were generated 500× in 2D and 3000× in 3D and angular deviation γ was extracted. Two regions were distinguished – the boundary layer where distance from the contact centroid to some boundary (parallel with the x axis) was lower than $l_{\min}$ and the interior containing all other contacts. The probability distributions of γ in these two groups are plotted in Fig. 3 together with the theoretical ideal distribution from Eq. (5). One can see that the interior has no directional bias while the boundary layer prefers elements aligned with the boundary.

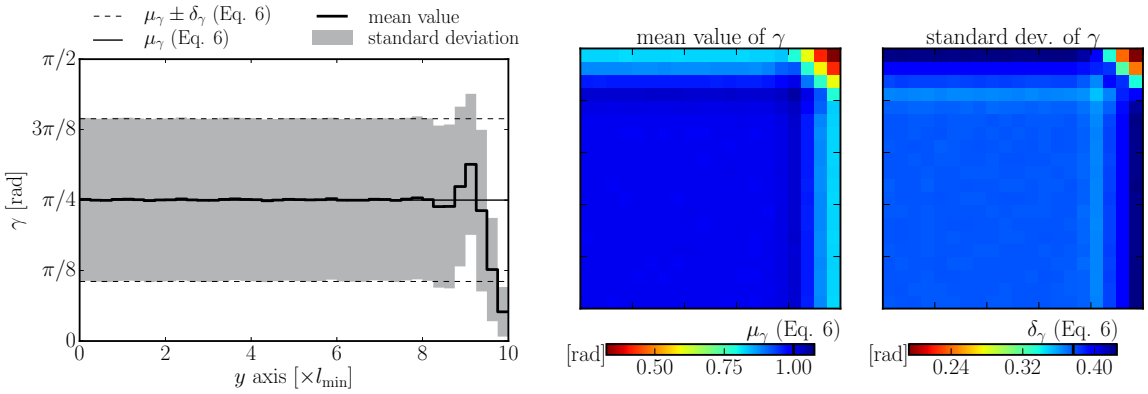

Figure 4: Statistical characteristics of the angular deviation from the x direction in 2D (left) & 3D (right) on symmetrical cross-section half or quarter, respectively.

To calculate the theoretical mean and standard deviation of γ, the distributions from Eq. (5) can be inserted into Eq. (1) and integrated for $g(\gamma) = \gamma$.

$$\mu_\gamma = \begin{cases} \dfrac{\pi}{4} & \text{2D} \\ 1 & \text{3D} \end{cases} \qquad \delta_\gamma = \begin{cases} \dfrac{\pi}{4\sqrt{3}} & \text{2D} \\ \sqrt{\pi - 3} & \text{3D} \end{cases} \tag{6}$$

These numbers are compared to an estimation of the mean and standard deviation calculated on the actual discrete systems in specimens from Fig. 2. Fig. 4 (left hand side) shows one symmetrical half of the cross section in the range $y = 0$ (center of the cross section) up to $y = 10 l_{\min}$ (boundary). The boundary layer exhibits a strong decrease in the mean indicating yet again that the elements are more aligned with the boundary. In 3D, Fig. 4 (right hand side) shows a symmetrical quarter of the cross section ranging from y, $z = 0$ (center of the cross section) up to y, $z = 5 l_{\min}$ (boundary). The bias in the boundary layer is similar to what was seen in 2D; it gets strongly emphasized in corners, where two perpendicular boundaries intersect.

5 ELASTIC BEHAVIOR

The prisms from the previous section were loaded by straining in the x direction (ε_{11}), while deformations in the y and z direction were unconstrained. Such loading results in a single tensorial stress component σ_{11} and the following strain components

$$\begin{array}{lll} \text{3D \& 2D plane stress} & \varepsilon_{11} = \dfrac{\sigma_{11}}{E} & \varepsilon_{22} = \varepsilon_{33} = -\dfrac{\nu \sigma_{11}}{E} = -\nu \varepsilon_{11} \\ \text{2D plane strain} & \varepsilon_{11} = \dfrac{\sigma_{11}(1-\nu^2)}{E} & \varepsilon_{22} = -\dfrac{\sigma_{11}(\nu+\nu^2)}{E} = \dfrac{\nu}{\nu-1}\varepsilon_{11} \end{array} \tag{7}$$

A simple assumption about the displacements and rotations of the bodies in the system when subjected to macroscopic uniform strain is now used. It is assumed that all the

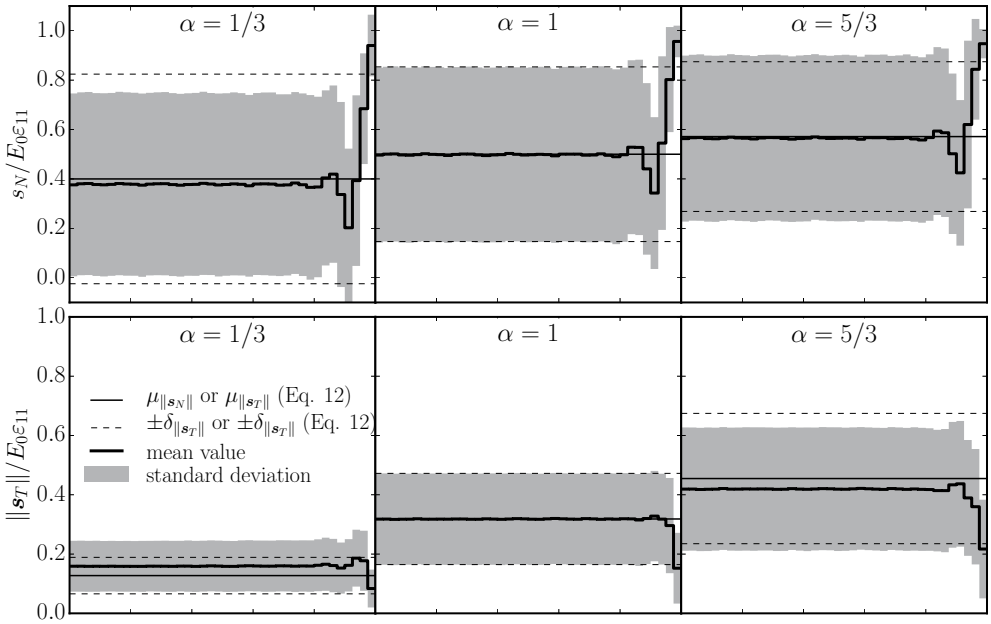

Figure 5: Average and standard deviation of normal stress (s_N, first row) and shear stress (s_T, second row) on a half cross section under tensile loading; 2D model, $\alpha = \{1/3,\ 1,\ 5/3\}$.

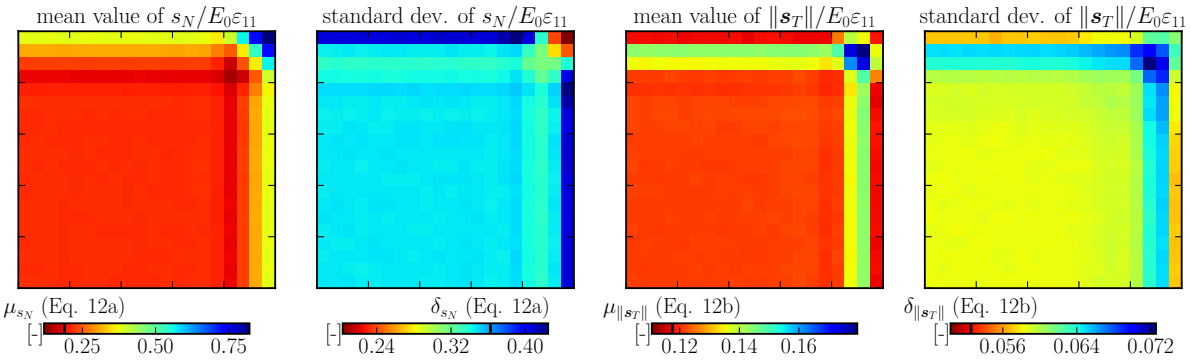

Figure 6: Average and standard deviation of the normal and shear stress on quarter cross-section; 3D model, $\alpha = 0.29$.

rotations are null ($\boldsymbol{\theta} = \boldsymbol{0}$) and the difference in displacements between any two nodes is

$$\boldsymbol{u}_b - \boldsymbol{u}_a = \boldsymbol{\varepsilon} \cdot (\boldsymbol{x}_b - \boldsymbol{x}_a) \tag{8}$$

Using assumption (8) and perpendicularity of the facet area to the element, the displacement jump is determined by the strain tensor

$$\boldsymbol{\Delta} = L\boldsymbol{\varepsilon} \cdot \boldsymbol{n} \tag{9}$$

Combining Eqs. (2)-(4), (7) and (9) the normal and tangential stress magnitude can be

evaluated

$$s_N = \varepsilon_{11} E_0 \left(\cos^2 \gamma - \frac{1-\alpha}{3+\alpha} \sin^2 \gamma \right) \tag{10}$$

$$\|\boldsymbol{s}_T\| = \varepsilon_{11} E_0 \alpha \sin \gamma \cos \gamma \frac{4}{3+\alpha} \tag{11}$$

The expression for the stress magnitudes is the same for both 2D simplifications and 3D. Now, the theoretical unbiased mean and standard deviation can be integrated with $g(\gamma) = s_N$ and $g(\gamma) = \|\boldsymbol{s}_T\|$ using Eq. 1

$$\mu_{s_N} = \begin{cases} \varepsilon_{11} E_0 \dfrac{1+\alpha}{3+\alpha} & \text{2D} \\ \varepsilon_{11} E_0 \dfrac{1+3\alpha}{3(3+\alpha)} & \text{3D} \end{cases} \qquad \delta_{s_N} = \begin{cases} \varepsilon_{11} E_0 \dfrac{\sqrt{2}}{3+\alpha} & \text{2D} \\ \varepsilon_{11} E_0 \dfrac{8}{3\sqrt{5}(3+\alpha)} & \text{3D} \end{cases} \tag{12a}$$

$$\mu_{\|\boldsymbol{s}_T\|} = \begin{cases} \varepsilon_{11} E_0 \alpha \dfrac{4}{\pi(3+\alpha)} & \text{2D} \\ \varepsilon_{11} E_0 \alpha \dfrac{4}{3(3+\alpha)} & \text{3D} \end{cases} \qquad \delta_{\|\boldsymbol{s}_T\|} = \begin{cases} \varepsilon_{11} E_0 \alpha \dfrac{\sqrt{2(\pi^2-8)}}{\pi(3+\alpha)} & \text{2D} \\ \varepsilon_{11} E_0 \alpha \dfrac{4}{3\sqrt{5}(3+\alpha)} & \text{3D} \end{cases} \tag{12b}$$

A comparison with a real discrete system behavior is shown for 2D and 3D in Figs. 5 and 6 for selected α parameters. The value $\alpha = 0.29$ has been chosen for 3D model because it is typical for concrete. The normal and shear stresses are normalized by $\varepsilon_{11} E_0$. One can see reasonable approximation of the stresses by analytical formulas (12a) and (12b) in the interior, the difference are caused by only approximate validity of the assumption (8). In the boundary layer, the normal stress increases while the shear stress decreases.

6 INELASTIC BEHAVIOR

A typical constitutive behavior, applied also here, is weaker and less ductile in tensile loading than in shear. Therefore, the boundary layer with a tendency of elements to be parallel to the boundary becomes weaker and more brittle under straining along its direction than the interior part.

The results are reported only for the 3D model with material parameters: $E_0 = 60\,\text{GPa}$, $\alpha = 0.29$, $f_\text{t} = 2.2\,\text{MPa}$ and $G_\text{t} = 35\,\text{J/m}^2$. These parameters were obtained in [11] by fitting a large experimental series [13] for $l_\text{min} = 10\,\text{mm}$. A periodic prisms of 200 mm in length (x axis) and square cross section of size 50 mm, 100 mm and 200 mm periodic in y and z directions are strained in uniaxial tension along the x direction.

The periodicity is used to remove the boundaries and the directional bias in its vicinity. To compare it with the bounded specimen, the boundaries are also introduced into the periodic structure by mirroring the nuclei across the xy and xz planes (Fig. 1c).

The nominal stress and elongation of the prisms are calculated 30 times with different geometry of the discrete structure and averaged. The averaged responses are shown in

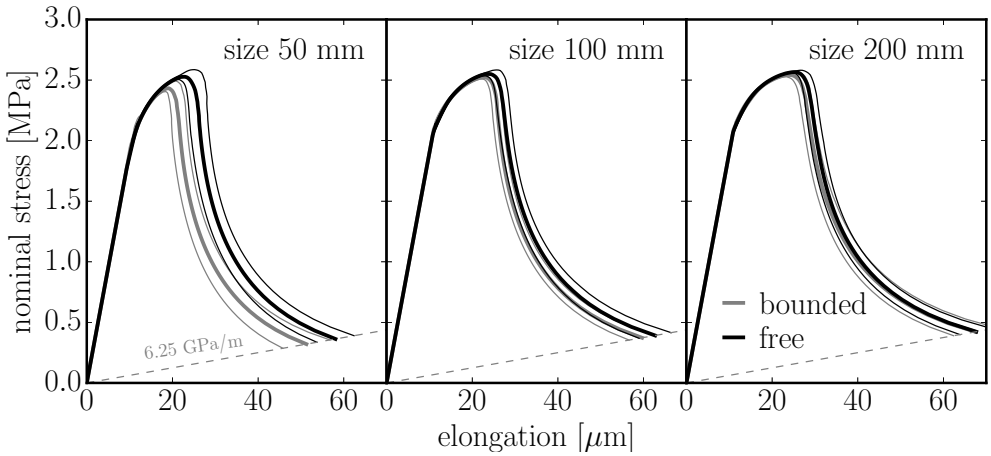

Figure 7: Averaged responses of periodic 3D model with (*bounded*) and without (*free*) boundaries loaded in pure tension

Fig. 7. The difference between the *bounded* and boundary *free* model decreases with size as the weak boundary layer occupies a lower portion of the specimen. In the worst case (the smallest specimen), the strength decreases by 4% and energy dissipation by 24% when boundaries are added.

7 CONCLUSIONS

The static discrete models with geometry of rigid bodies generated by Voronoi tessellation on randomly placed nuclei are studied. The standard elastic and inelastic contact behavior is applied.

- The contribution demonstrates the bias in the orientation of elements in the boundary layer. Contacts parallel to the boundary are represented with higher probability than what an unbiased model shall exhibit.
- Consequence of the orientation bias is that the elastic behavior of the boundary layer differ from the interior. When straining parallel to the boundary, the shear components are more relaxed while the normal components are loaded more compared to the elastic behavior of the interior. Therefore, for positive Poisson's ratios, the boundary layer becomes stiffer and vice versa.
- When the inelastic behavior has a typical form having both strength and fracture energy in the normal direction lower than in shear, the boundary layer becomes also weaker and less ductile.

Acknowledgement

The financial support provided by the Czech Science Foundation under project No. 15-19865Y is gratefully acknowledged.

REFERENCES

[1] Eliáš, J. Boundary layer effect on behavior of discrete models. *Materials* (2017) **10**:157.

[2] Bažant, Z.P. and Planas, J. *Fracture and size effect in concrete and other quasibrittle materials*. Boca Raton, Florida, USA: CRC Press (1997).

[3] Vořechovský, M. and Sadílek, V. Computational modeling of size effects in concrete specimens under uniaxial tension. *Int. J. Fracture* (2008) **154**:27–49.

[4] Havlásek, P., Grassl, P. and Jirásek, M. Analysis of size effect on strength of quasi-brittle materials using integral-type nonlocal models. *Eng. Fract. Mech.* (2016) **157**:72–85.

[5] Asahina, D., Ito, K., Houseworth, J.E., Birkholzer, J.T. and Bolander, J.E. Simulating the Poisson effect in lattice models of elastic continua. *Comput. Geotech.* (2015) **70**:60–67.

[6] Asahina, D., Aoyagi, K., Kim, K., Birkholzer, J.T. and Bolander, J.E. Elastically-homogeneous lattice models of damage in geomaterials. *Comput. Geotech.* (2017) **81**:195–206.

[7] Cusatis, G., Rezakhani, R. and Schauffert, E.A. Discontinuous Cell Method (DCM) for the simulation of cohesive fracture and fragmentation of continuous media. *Eng. Fract. Mech.* (2017) **170**:1–22.

[8] Berton, S. and Bolander, J.E. Crack band model of fracture in irregular lattices. *Comput. Method. Appl. M.* (2006) **195**:7172–7181.

[9] Bolander, J.E., Hong, G.S. and Yoshitake, K. Structural concrete analysis using rigid-body-spring networks. *Comput.-Aided Civ. Inf.* (2000) **15**:120–133.

[10] Cusatis, G. and Cedolin, L. Two-scale study of concrete fracturing behavior. *Eng. Fract. Mech.* (2007) **74**:3–17.

[11] Eliáš, J. Adaptive technique for discrete models of fracture. *Int. J. Solids Struct.* (2016) **100-101**:376–387.

[12] Kuhl, E., D'Addetta, G.A., Herrmann, H.J. and Ramm, E. A comparison of discrete granular material models with continuous microplane formulations. *Granul. Matter* (2000) **2**:113–121.

[13] Grégoire, D., Rojas-Solano, L.B. and Pijaudier-Cabot, G. Failure and size effect for notched and unnotched concrete beams. *Int. J. Numer. Anal. Met.* (2013) **37**:1434–1452.